



Development of a joint hydrogeophysical inversion approach and application to a contaminated fractured aquifer

J. Chen,¹ S. Hubbard,¹ J. Peterson,¹ K. Williams,¹ M. Fienen,² P. Jardine,³ and D. Watson³

Received 26 October 2005; revised 24 February 2006; accepted 13 March 2006; published 30 June 2006.

[1] This paper presents a joint inversion approach for combining crosshole seismic travel time and borehole flowmeter test data to estimate hydrogeological zonation. The approach is applied to a complex, fractured Department of Energy field site located at the Oak Ridge National Laboratory in Tennessee, United States. We consider seismic slowness (the inverse of seismic velocity) and hydrogeological zonation indicators as unknown variables and use a physically based model with unknown parameters to relate the seismic slowness to the zonation indicators. We jointly estimate all the unknown parameters in the model by conditioning them to the crosshole seismic travel times as well as the borehole flowmeter data using a Bayesian model and a Markov chain Monte Carlo sampling method. The fracture zonation estimates are qualitatively compared to bromide tracer breakthrough data and to uranium biostimulation experiment results. The comparison suggests that the joint inversion approach adequately estimated the fractured zonation and that the fracture zonation influenced biostimulation efficacy. Our study suggests that the new joint hydrogeophysical inversion approach is flexible and effective for integrating various types of data sets within complex subsurface environments and that seismic travel time data have the potential to provide valuable information about fracture zonation.

Citation: Chen, J., S. Hubbard, J. Peterson, K. Williams, M. Fienen, P. Jardine, and D. Watson (2006), Development of a joint hydrogeophysical inversion approach and application to a contaminated fractured aquifer, *Water Resour. Res.*, 42, W06425, doi:10.1029/2005WR004694.

1. Introduction

[2] Crosshole geophysical techniques, such as seismic, ground-penetrating radar (GPR), and electrical resistivity tomography (ERT), have been increasingly used for characterizing subsurface properties and for monitoring subsurface processes. This is because geophysical tomographic data have the potential to provide high-resolution information about subsurface properties at locations away from boreholes in a minimally invasive manner. Conventional approaches for combining crosshole geophysical data and borehole hydrogeological measurements usually entail two sequential steps. First, the crosshole geophysical measurements (such as seismic or radar travel times) are inverted for geophysical attributes (such as seismic or GPR velocity values) at each pixel in space using a geophysical inversion algorithm [e.g., Peterson *et al.*, 1985]. Second, the inverted geophysical attributes are combined with the borehole hydrogeological measurements using various integration methods, for example, direct mapping [e.g., Hubbard *et al.*, 1997; Binley *et al.*, 2001], geostatistical cokriging [e.g.,

Cassiani *et al.*, 1998], or Bayesian methods [e.g., Chen *et al.*, 2001, 2004].

[3] The two-step approaches are generally effective when good site-specific petrophysical relationships between the inverted geophysical attributes and the hydrogeological properties are easily obtainable, and when the developed petrophysical relationships are approximately uniform over the region of interest. However, they are ineffective or even fail in some situations, such as when geophysical inversion errors are large or when petrophysical models are difficult to obtain. It has been well recognized that the inverted tomographic data are subject to uncertainty and artifacts, are often overly smooth, and have spatially varied resolution [Day-Lewis and Lane, 2004], which are functions of measurement errors, geometry of the interwell region, and the heterogeneity of subsurface properties [e.g., Vasco *et al.*, 1996; Peterson, 2001]. It has also been recognized that petrophysical relationships between geophysical attributes and hydrogeological parameters may intrinsically be non-unique and nonstationary [Linde *et al.*, 2006]. Consequently, treating the inverted geophysical attributes as data, and using a stationary petrophysical relationships for integration of geophysical and hydrogeological data sets may lead to biased estimates of the hydrogeological parameters.

[4] Joint inversion of geophysical and hydrogeological data for subsurface hydrogeological parameter estimation has received much attention recently. For example, Hyndman *et al.* [1994] jointly inverted seismic travel time and tracer experiment data for hydraulic conductivity zonation.

¹Lawrence Berkeley National Laboratory, Berkeley, California, USA.

²Department of Civil and Environmental Engineering, Stanford University, Stanford, California, USA.

³Environmental Sciences Division, Oak Ridge National Laboratory, Oak Ridge, Tennessee, USA.

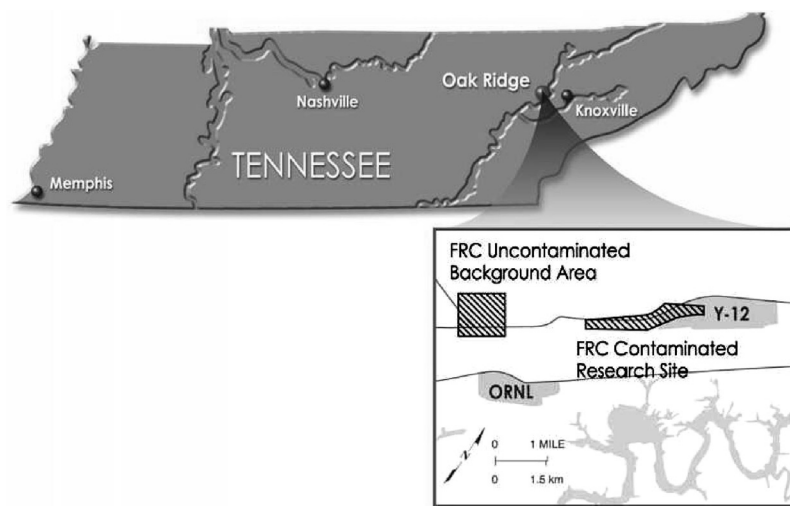


Figure 1. Location of the NABIR Field Research Center (FRC) near Oak Ridge, Tennessee [Watson et al., 2005]. Shaded lines indicate major rivers in the state of Tennessee.

tion using the split inversion method (SIP), and Kowalsky et al. [2004] jointly inverted ground-penetrating radar (GPR) travel time and borehole water saturation measurements for permeability estimation in the vadose zone using the maximum a posteriori (MAP) method. Both studies used optimization-based methods for solving unknown parameters. However, those methods have limitations when the number of unknowns involved is very large and geophysical and hydrogeological forward models are complex.

[5] In this study, we develop a joint inversion approach using a sampling-based stochastic model to integrate crosshole seismic travel time and borehole flowmeter test data for characterizing hydrogeological zonation in a complex fractured aquifer. Sampling-based stochastic methods have been used recently by other researchers to jointly invert geophysical data [Bosch et al., 2001; Malinverno, 2002; Buland and Omre, 2003]. We apply the developed model to data sets collected from a fractured Department of Energy (DOE) field site located at the Department of Energy (DOE) Oak Ridge Reservation in Tennessee. The conventional two-step approach was unsuccessful at this field site because petrophysical relationships between the inverted seismic slowness and the hydraulic conductivity were not obtainable from the colocated data. To improve the characterization, we jointly consider crosshole seismic travel time (rather than inverted seismic slowness) and borehole flowmeter test measurements as data, and consider seismic slowness and hydrogeological zonation indicators at each pixel as unknown random variables. With the hydrogeological indicator approach, we seek to estimate zones that have either relatively high or low hydraulic conductivity. We use a probabilistic petrophysical model with unknown parameters to link seismic slowness to hydrogeological zonation. Within a Bayesian framework, the unknown variables and parameters are simultaneously estimated using Markov chain Monte Carlo (MCMC) methods by conditioning them to crosshole seismic travel time and borehole flowmeter data. Although the methodology is developed on the basis of crosshole seismic travel time data collected within a fractured aquifer, the developed framework could be used with

other geophysical data sets (such as crosshole GPR) for other hydrogeological characterization objectives.

[6] The remainder of this paper is organized as follows. Section 2 describes the field site and available data. Section 3 describes the developed Bayesian model. Section 4 describes our MCMC sampling method for solving the developed statistical model. Application of the developed methodology is given in section 5, and a summary is provided in section 6.

2. Site Information and Data

2.1. Study Site

[7] The Field Research Center (FRC) of the Natural and Accelerated Bioremediation Research Program (NABIR) is located on the DOE Oak Ridge Reservation in Tennessee (Figure 1). Underlying the research center is the Nolichucky Shale bedrock that dips approximately 27 degrees to the southeast and has a geological strike of N58E [Fioren et al., 2005]. Our investigation was performed at FRC Area 3, where ongoing research is focused on developing and evaluating biostimulation techniques for remediation of U(VI) within the near subsurface materials [Criddle et al., 2003; Wu et al., 2006a, 2006b].

[8] Overlying the Nolichucky Shale bedrock is unconsolidated materials that consist of weathered bedrock (referred to as saprolite) and a thin layer of human-placed fill near the surface. The fill is too shallow and thin (1–2 m thick) to have an impact on the zones targeted during this study. The saprolite overlying the Nolichucky Shale is approximately 13 m thick at the study site. To a depth of approximately 10 m, the saprolite is clay-rich and has a low permeability [Watson et al., 2005]. Between the shallow, low-permeability clay-rich saprolite and deeper competent bedrock is a transition zone of fractured bedrock that has been weathered to varying degrees. Remnant fracturing in the clayey saprolite and transition zone increases the permeability relative to the silt, clay, and rock matrix. The transition zone tends to be a zone of higher permeability than the saprolite and bedrock because of a combination of higher fracture density and low clay content. Understanding

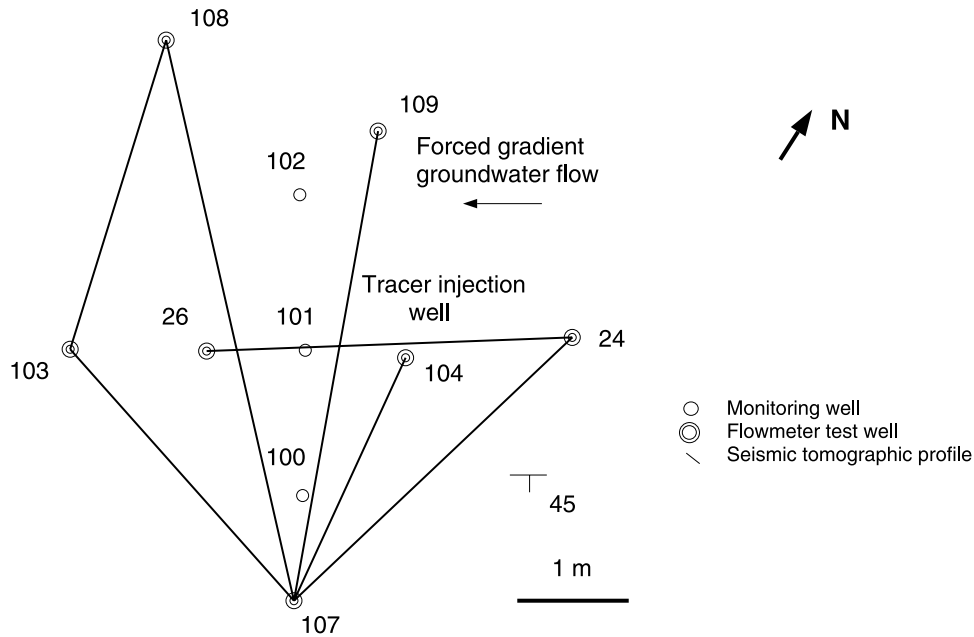


Figure 2. Geometry and locations of borehole and seismic tomographic data at the FRC Area 3 study site.

the distribution of high-permeability flow zones within the saprolite transition zone is critical to the understanding of contaminant fate and transport at the site for optimal design of remedial treatments.

2.2. Crosshole Seismic Travel Time Data

[9] Surface and crosshole geophysical techniques have been used to characterize subsurface properties at the FRC Area 3 site over various spatial scales. For the initial investigations, surface resistivity surveys and seismic refraction tomography were used to image the large-scale subsurface geological structure [Doll et al., 2002]. To characterize heterogeneity and to potentially estimate the hydrogeological properties at the local scale, we collected high-resolution crosshole seismic data along several transects as is shown in Figure 2.

[10] Seismic tomographic acquisition includes placing seismic sources and receivers (geophones) in two separate boreholes. Seismic waves from the sources in one borehole are recorded by the receivers in the other borehole. The source and receiver positions are changed and the recording is repeated until both the sources and the receivers have occupied all possible positions within the two boreholes. Crosshole seismic travel time data were collected using a central frequency of 4 KHz with a bandwidth from approximately 1 KHz to 7 KHz. Both seismic P wave travel times between all pairs of the source/receiver positions and the amplitude of the direct arrivals were obtained from the recorded data. The measured seismic travel time data can be inverted by using deterministic geophysical inversion algorithms, such as the method used by Peterson et al. [1985], to obtain tomographic seismic slowness (or velocity) at each pixel along the two-dimensional cross section. Figure 3 shows the inverted seismic tomograms along geological dip and strike directions. At a depth between 11–13 m is a low-velocity lens, which is the target zone for the FRC Area 3 biostimulation experiment.

2.3. Borehole Flowmeter Test Data

[11] Subsurface hydraulic conductivity estimates at this site (Figure 2) were obtained using data collected from the pumping test carried out at well 24 and the flowmeter tests conducted within several boreholes. The pumping test provides information about depth averaged hydraulic conductivity, whereas the flowmeter tests provide information on the relative values of hydraulic conductivity at various

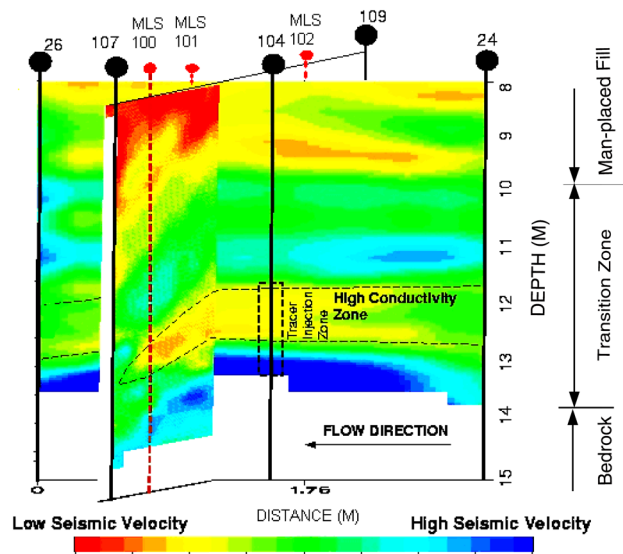


Figure 3. Conventionally inverted seismic velocity along the geological dip (approximately 107-109) and strike directions (24-26) in the saturated section. In this study, we focus on an area between 10 and 14 m, which contains a high-conductivity zone that is the target of the biostimulation experiment.

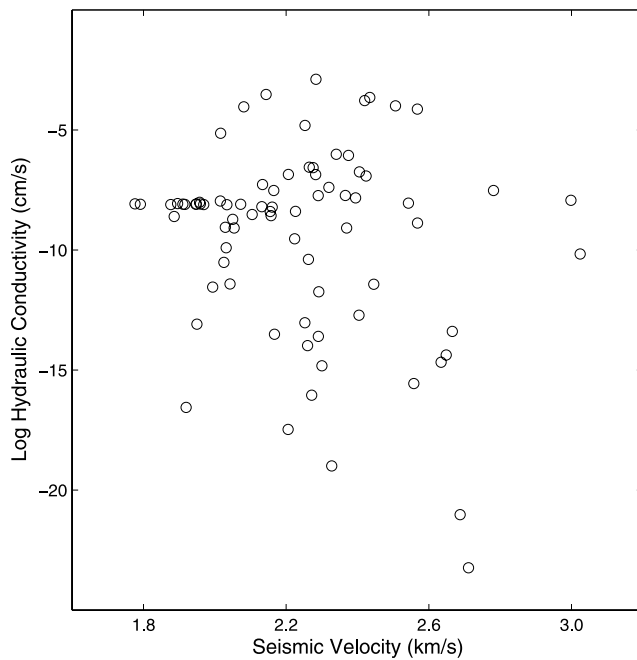


Figure 4. Cross plot between the inverted seismic velocity and logarithmic hydraulic conductivity showing the poor correlation obtained using conventional approaches.

discrete intervals along the depths between 3 and 16 m. The sampling intervals of the flowmeter tests vary from 0.03 m to 0.60 m. Both traditional deterministic methods [Molz *et al.*, 1994] and Bayesian inversion methods [Fienen *et al.*, 2004] were used to estimate hydraulic conductivity values as a function of depth from the combined slug and flowmeter test data at the site. The hydraulic conductivity values at this site range from 2.0×10^{-12} cm/s to 1.7×10^{-1} cm/s, with a median value of 2.8×10^{-5} cm/s. However, from the flowmeter test data, we observed that there are essentially two zones in each well, a flow zone and a zone of almost no flow. The maximum value of hydraulic conductivity in the zone of little or no flow is about 1.0×10^{-4} cm/s. Therefore we chose the hydraulic conductivity value of 1.0×10^{-4} cm/s, rather than the median (2.8×10^{-5} cm/s), as

the cutoff value between the flow zone and the zone of no flow. We define conductivities greater or equal to 1.0×10^{-4} cm/s as “high” and conductivities less than 1.0×10^{-4} cm/s as “low.” The threshold value of 1.0×10^{-4} cm/s is the same as found by Ellefsen *et al.* [2002] for the fractured bedrock near Mirror Lake in New Hampshire.

2.4. Relationship Between Seismic Velocity and Hydraulic Conductivity

[12] Following the conventional approach, we first develop petrophysical models on the basis of the inverted seismic tomograms (Figure 3) and borehole hydraulic conductivity data. Figure 4 shows the cross correlation between the inverted seismic velocity near boreholes and the logarithmic hydraulic conductivity at boreholes from depths 10 m to 14 m. The poor correlation is not surprising because we observed seismic anisotropy at this site. For example, Figure 5 shows the inverted seismic velocity as a function of depth at well 24, which were extracted from two different seismic tomograms: 107-24 and 26-24 (see Figure 2). Figure 2 reveals that although the changes in seismic velocity as a function of depth are similar (i.e., the low seismic velocity and high-conductivity zones are located approximately at the same depths), the direction of the tomograms influences the absolute values of the inverted seismic velocity. Such angle dependency of inverted seismic velocity results in a poor correlation between seismic velocity and hydraulic conductivity. As is illustrated in Figure 4. With the poor correlation, it is difficult to develop an empirical petrophysical relationship to obtain quantitative information about hydraulic conductivity from the inverted seismic tomograms.

[13] We do, however, expect seismic velocity to be qualitatively related to hydraulic conductivity in fractured media because both are affected by the geometry of the void space of fracture networks [Pyrak-Nolte *et al.*, 1990]. Seismic velocity is a function of elastic stiffness and bulk density of the medium, which is typically low for high fracture density and high for low fracture density. Flow properties are functions of void space and connectivity of the void space, and the aquifer materials with high fracture density tend to have high hydraulic conductivity. Conse-

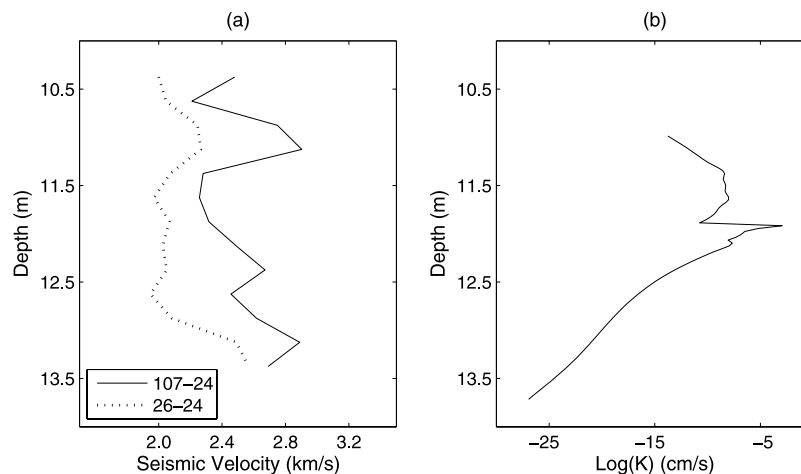


Figure 5. (a) Seismic velocity extracted from transects 107-24 and 26-24 near well 24. (b) Hydraulic conductivity collected from well 24.

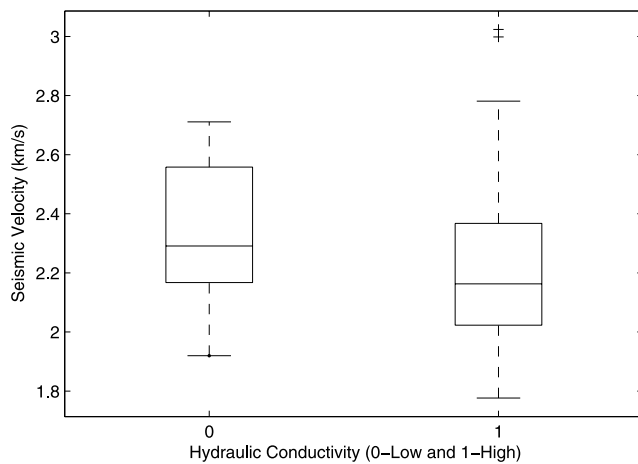


Figure 6. Box plot of the inverted seismic velocity.

quently, fractured subsurface materials with low seismic velocity likely have high hydraulic conductivity. However, since seismic velocity is a measure of the effective mechanical properties of the medium and the hydraulic behavior of the medium is not entirely governed by its mechanical properties, the relationship between seismic velocity and hydraulic conductivity is nonunique and subject to uncertainty [Majer *et al.*, 1990, 1997]. In addition, since quantitative correlation between the geometry and density of fractures and hydraulic conductivity in field conditions has not been established [Illman, 2005; Illman and Neuman, 2000], we focus on estimating hydrogeological zonation in this study.

[14] The physical connection between seismic velocity and hydraulic conductivity in fractured media described above is supported by data collected from the FRC site. Figure 6 shows a box plot between the inverted seismic velocity and the indicator values (0 = low and 1 = high) of hydraulic conductivity, based on data collected from all the wells shown in Figure 2. Although the inverted seismic velocity is subject to a large degree of uncertainty, the mean seismic velocity of the high-conductivity zone is lower than that of the low-conductivity zone, with a ratio of about 1.05. Similar results were also observed using seismic data collected from the fractured bedrock near the Mirror Lake in New Hampshire [Ellefsen *et al.*, 2002]. We also performed the t test for the difference in the mean seismic velocity and found it is statistically significant with the cutoff value of 0.05.

[15] Since the inverted seismic velocity data are affected by the orientation of transects and the relationship between the seismic velocity and the hydraulic conductivity are thus subject to uncertainty, we follow an approach that is different from our previous hydrogeological parameter estimation approaches developed for porous media [Chen *et al.*, 2001]. First, we estimate the zonation indicator rather than continuous value of hydraulic conductivity at each pixel in space. Second, we consider crosshole seismic travel times instead of inverted seismic slowness as data, and consider seismic slowness and zonation indicator at each pixel as random variables. This should reduce the effect of uncertainty associated with seismic travel time data inversion because we can combine some information from boreholes with seismic data in a joint inversion procedure.

Finally, we use a probabilistic model to link the unknown seismic slowness to the unknown zonation indicator values at each pixel. We assume that seismic slowness in the high- and low-conductivity zones is normally distributed with unknown variances and unknown means. We also assume that the ratio of mean conductivity values between the high and low zones is available, which is site-specific and derived from nearby borehole data. As will be illustrated in section 5, our joint inversion approach yields estimates of seismic slowness and zonation indicators at each pixel, as well as the means and variances of seismic slowness in the high- and low-conductivity zones.

3. Joint Hydrogeophysical Inversion Approach

[16] This section describes the methodology that we developed to characterize the fracture zonation at the FRC study site given crosshole seismic travel time and borehole flowmeter test data. We estimate the probability of encountering the high-conductivity fracture zone (i.e., indicator = 1) at each pixel between boreholes using a Bayesian framework, where the seismic slowness and zonation indicator at each pixel in space are considered as random variables. The petrophysical models between seismic slowness and zonation indicator include unknown parameters that are estimated during the inversion approach. The unknown parameters, as well as the unknown slowness and zonation indicators, will be estimated jointly by conditioning to both seismic travel time and flowmeter test data. In this section, we focus on the development of the Bayesian framework, and the sampling methods that we use for solving those unknown variables are described in section 4.

3.1. Bayesian Model

[17] We develop a Bayesian model to combine crosshole seismic travel time data with borehole indicator values of flowmeter test data. For example, in the case of well pair 107-109 shown in Figure 7, the available data include seismic travel times obtained from waveforms recorded at well 109 and zonation indicator values of hydraulic conductivity at wells 107 and 109. We divide the cross section between the two wells into n pixels, and m seismic ray paths pass through the cross section. Let K_i and S_i denote the hydraulic conductivity zonation indicator and the seismic slowness at pixel- i , respectively, where $i = 1, 2, \dots, n$. Let t_j denote the seismic travel time measurement of the j th ray

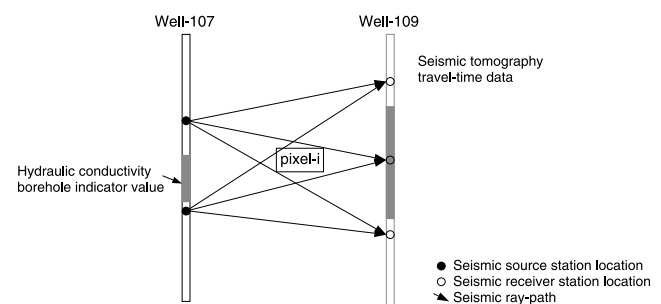


Figure 7. Schematic diagram of the model setup, where the gray areas in the boreholes represent the high-conductivity zone, and the open areas in the boreholes represent the low-conductivity zone.

path, where $j = 1, 2, \dots, m$. Let $\{k_w\}$ denote the indicator values of all the flowmeter test data.

[18] Our objective is to estimate the conditional probability distributions of seismic slowness and zonation indicators, given the crosshole seismic travel time data and the indicator values of borehole flowmeter data. Let squared brackets represent probability functions for discrete random variables and probability density functions (pdfs) for continuous random variables. Let other brackets $\{\}$ represent vectors. With this notation, our Bayesian model can be written as

$$[\{S_i\}, \{K_i\}, \tau_s, \Theta | \{t_j\}, \{k_w\}] \propto [\{S_i\}, \{K_i\}, \tau_s, \Theta, \{k_w\}] \cdot [\{t_j\} | \{S_i\}, \tau_s], \quad (1)$$

where τ_s denotes the inverse variance of the travel time measurement errors, and Θ is a vector including all the unknown parameters associated with a petrophysical model, which are specified later in this section. Equation (1) ignores a constant that does not depend on the unknown variables. The first term on the right side of the equation is referred to as the prior model, and the second term is referred to as the likelihood model. Those models are described in sections 3.2 and 3.3, respectively.

3.2. Prior Model

[19] The prior model summarizes all information about the unknown variables that are not included in seismic travel time data. For application at the FRC site, we must specify a petrophysical model that links the seismic slowness to the zonation indicator at each pixel. As was mentioned in section 2.4, we assume that seismic slowness within the high- or low-conductivity zones has a normal distribution with unknown means and variances. We denote u and w as the mean seismic slowness values in the low- and high-conductivity zones, respectively, and assumes that $u < w$.

[20] For simplicity, we also assume that the ratio between the mean seismic slowness in the high- and low-conductivity zones is a constant. We determine the ratio using collocated flowmeter and inverted seismic slowness data. We can relax this assumption by allowing the ratio to be changed within a small range, for example, as a function of direction, which is justified because the relative values of seismic slowness are more stable than their corresponding absolute values. The absolute estimates of seismic slowness are affected by many factors, such as seismic inversion methods, model discretization, and the distance between two boreholes [Peterson, 2001]. If we write $w = u + ru$, variable r will be equal to 0.05 on the basis of Figure 6 as given in section 2.4. Let τ_k be the inverse variance of seismic slowness in the low- and high-conductivity zones. Therefore the unknown parameters associated with the petrophysical model include u and τ_k , that is, $\Theta = (u, \tau_k)$.

[21] Figure 8 shows dependence among various unknown variables and parameters. The probabilistic petrophysical model for linking collocated seismic slowness and zonation indicators is given by

$$[S_i | K_i, u, \tau_k] = \frac{1}{\sqrt{2\pi}} \tau_k^{1/2} \exp\left\{-\frac{\tau_k}{2} (S_i - u - ruK_i)^2\right\}. \quad (2)$$

Equation (2) implies that seismic slowness in the low-conductivity zone ($K_i = 0$) is normally distributed with mean

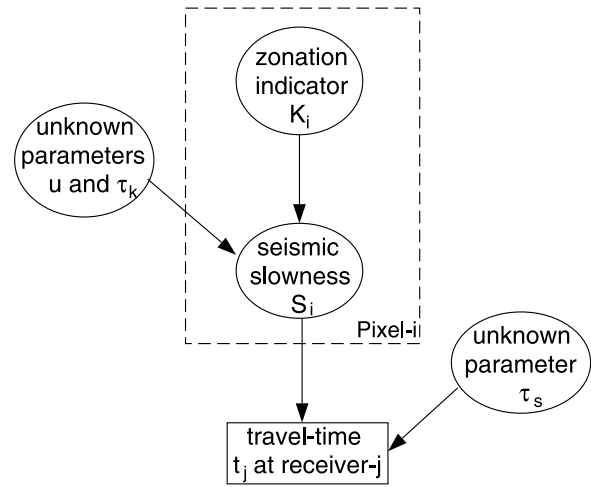


Figure 8. Dependence among seismic slowness, zonation indicator, and parameters associated with the petrophysical model. The circles represent unknown variables, and the rectangle represents the given data.

u , and seismic slowness in the high-conductivity zone ($K_i = 1$) is normally distributed with mean $w = u + ru$. If we assume that the seismic slowness at pixel i is independent of those at other pixels given its collocated indicator value K_i , and $\{K_i\}$, u , τ_k , and τ_s are also independent of one another, the prior model in equation (1) thus is given by

$$[\{S_i\}, \{K_i\}, u, \tau_k, \tau_s, \{k_w\}] \propto [\{K_i\}, \{k_w\}] [u] [\tau_k] [\tau_s] \prod_{i=1}^n [S_i | K_i, u, \tau_k]. \quad (3)$$

Equation (3) also ignores a constant that is not dependant on the unknown variables. The detailed distributions of variables K_i , u , τ_k , and τ_s are given in section 4.

3.3. Likelihood Model

[22] We develop the likelihood model in equation (1) on the basis of a straight ray path forward model [Peterson *et al.*, 1985], which connects crosshole seismic travel time data recorded along boreholes to seismic slowness at pixels on the cross section. In this model, seismic travel time along a given ray path is simply the summation of the product of the slowness and the length of the ray path passing through a pixel. Let a_{ij} denote the length of the j th ray passing through the i th pixel, and ϵ_j denote the measurement error of the travel time along the j th ray path. Thus travel time t_j is given by

$$t_j = \sum_{i \in C_j} a_{ij} S_i + \epsilon_j, \quad (4)$$

where C_j is a collection of pixel indices that the j th ray path passes through. Suppose that measurement errors of seismic travel times have a normal distribution with zero mean and the inverse variance of τ_s . The likelihood function for the j th travel time measurement is then given by

$$[t_j | \{S_i\}, \tau_s] = \frac{1}{\sqrt{2\pi}} \tau_s^{1/2} \exp\left\{-\frac{\tau_s}{2} \left(t_j - \sum_{i \in C_j} a_{ij} S_i\right)^2\right\}. \quad (5)$$

[23] To facilitate the incorporation of equation (5) into the posterior estimation procedure described below, we regroup the terms in the small brackets. We divide those terms into two parts: one is related to S_i and the other is not related to S_i . Let $b_{ij} = t_j - \sum_{l \in C_j, l \neq i} a_{lj} S_l$, where l is a pixel index. The term b_{ij} is not related to S_i . This equation can be written as follows:

$$[t_j | \{S_i\}, \tau_s] = \frac{1}{\sqrt{2\pi}} \tau_s^{1/2} \exp\left\{-\frac{\tau_s}{2} (a_{ij} S_i - b_{ij})^2\right\}. \quad (6)$$

3.4. Posterior Model

[24] A posterior model can be obtained once the prior and likelihood models are specified. By assuming each travel time measurement is independent of others and using equations (3) and (6), we obtain the posterior model as follows:

$$\begin{aligned} [\{S_i\}, \{K_i\}, u, \tau_k, \tau_s | \{t_j\}, \{k_w\}] &\propto [\{K_i\}, \{k_w\}] [u] [\tau_s] [\tau_k] \prod_{i=1}^n \\ &\cdot [S_i | K_i, u, \tau_k] \prod_{j=1}^m [t_j | \{S_i\}, \tau_s]. \end{aligned} \quad (7)$$

[25] Equation (7) is a joint posterior distribution. Our goal is to obtain estimates of each unknown variable from this joint posterior distribution at each pixel in space using a sampling-based procedure.

4. Sampling Method

[26] The section outlines an approach for estimating unknown seismic slowness and zonation indicators, as well as the unknown parameters associated with the petrophysical model, from the joint posterior distribution shown in equation (7). With this approach, we strive to obtain many samples of unknown variables using an algorithm similar to the one used by *Chen et al.* [2004]. As will be described below, we first derive the conditional distribution of each unknown variable given the travel time data and all the other variables, which is referred to as the full conditional distribution of the variable. We then sequentially draw samples from each full conditional distribution. We monitor the convergence of the sampling procedure using the method developed by *Gelman and Rubin* [1992]. After convergence, we can calculate the mean, variance, predictive intervals, and even density or probability function of each variable from those samples.

4.1. Deriving Full Conditional Distributions

[27] A full conditional distribution of any variable is proportional to the joint posterior distribution shown in equation (7) on the basis of Bayes' theorem [*Bernardo and Smith*, 1994]. By omitting the terms at the right side of equation (7) that are not directly related to the variable under consideration, we can obtain the full conditional distribution of each variable individually as described below.

4.1.1. Full Conditional PDF of S_i

[28] Let $[S_i | \cdot]$ denote the full conditional pdf of slowness S_i given the travel time data and all other variables. After

omitting all the terms in equation (7) that are not directly related to S_i , we obtain

$$[S_i | \cdot] \propto [S_i | K_i, u, \tau_k] \prod_{j \in D_i} [t_j | \{S_i\}, \tau_s], \quad (8)$$

where D_i is the index set of all the ray paths passing through the i th pixel. By using equations (2) and (6) in equation (8), and omitting the terms not including S_i , we obtain

$$[S_i | \cdot] \propto \exp\left\{-\frac{\tau_k}{2} (S_i - u - r u K_i)^2\right\} \exp\left\{-\frac{\tau_s}{2} \sum_{j \in D_i} (a_{ij} S_i - b_{ij})^2\right\}. \quad (9)$$

[29] From equation (9), we found that $[S_i | \cdot]$ has the normal distribution with the mean (μ_s^*) and inverse variance (τ_s^*) given by

$$\tau_s^* = \sum_{j \in D_i} a_{ij}^2 \tau_s + \tau_k \quad (10)$$

$$\mu_s^* = \left(\sum_{j \in D_i} a_{ij} b_{ij} \tau_s + (u + r u K_i) \tau_k \right) / \tau_s^*. \quad (11)$$

4.1.2. Full Conditional Probability of K_i

[30] Similar to the derivation of $[S_i | \cdot]$, the full conditional probability function of the hydraulic conductivity, K_i , is given by

$$[K_i | \cdot] \propto [S_i | K_i, u, \tau_k] [K_i | \{K_j, j \neq i\}, \{k_w\}], \quad (12)$$

where $\{K_j, j \neq i\}$ denotes the zonation indicators at the pixels surrounding the i th pixel. Inserting equation (2) into equation (12), and using identity equation $K_i^2 = K_i$, we obtain

$$[K_i | \cdot] \propto \exp\{\tau_k u r K_i (S_i - 0.5 u r - u)\} [K_i | \{K_j, j \neq i\}, \{k_w\}], \quad (13)$$

We assume that zonation K_i depends only on the zonation at its adjacent pixels [*Chen and Rubin*, 2003]. Let set A_i be the index set of the pixels adjacent to pixel i . For those pixels not near boreholes, the conditional probability of K_i does not depend on borehole zonation measurements, and thus it is given by

$$[K_i | \{K_j, j \neq i\}, \{k_w\}] = [K_i | K_j, j \in A_i] \sim \text{Bernoulli}(p^*), \quad (14)$$

where p^* is the probability of zonation having high conductivity given the zonation at its surrounding pixels, which was obtained for our study using the same indicator kriging method as used by *Chen et al.* [2004]. Equation (14) is immediately applicable for those pixels near boreholes, when we replace zonation indicator variables at pixels in boreholes with the borehole flowmeter measurements. Consequently, $[K_i | \cdot]$ has a Bernoulli distribution with probability p_i given by

$$p_i = \frac{p^* \exp\{\tau_k u r (S_i - 0.5 u r - u)\}}{1 - p^* + p^* \exp\{\tau_k u r (S_i - 0.5 u r - u)\}}. \quad (15)$$

4.1.3. Full Conditional PDFs of Parameters τ_k , τ_s , and u

[31] We first derive full conditional pdfs of τ_s . Notice from equation (7) that

$$[\tau_s|\cdot] \propto [\tau_s] \prod_{j=1}^m [t_j | \{S_j\}, \tau_s]. \quad (16)$$

Since τ_s only takes a positive value, we assume the prior distribution of τ_s has gamma distribution with shape parameter α_s and inverse-scale parameter λ_s , both of which are determined from our prior knowledge about τ_s . Let $T_s = \sum_{j=1}^m (t_j - \sum_{l \in C_j} a_{lj} S_l)^2$. By using equation (5), we obtain

$$[\tau_s|\cdot] \propto \tau_s^{\alpha_s-1} \exp\{-\lambda_s \tau_s\} \tau_s^{0.5m} \exp\{-0.5T_s \tau_s\} \\ \sim \text{Gamma}(\alpha_s + 0.5m, \lambda_s + 0.5T_s). \quad (17)$$

Similarly, let $T_k = \sum_{i=1}^n (S_i - u - r u K_i)^2$. Since τ_k only allows for positive values, we assume that the prior distribution of τ_k also has a gamma distribution with shape parameter α_k and inverse-scale parameter λ_k . The full conditional pdf of τ_k thus is the gamma distribution with shape parameter $\alpha_k + 0.5n$ and inverse-scale parameter $\lambda_k + 0.5T_k$.

[32] From equation (7), we know that

$$[u|\cdot] \propto [u] \prod_{i=1}^n [S_i | K_i, u, \tau_k]. \quad (18)$$

Suppose the prior distribution of u is the normal with mean u_0 and the inverse variance of τ_0 . The full conditional pdf of u thus is the normal distribution with mean (μ_u^*) and inverse variance (τ_u^*) given as below:

$$\tau_u^* = \tau_k \sum_{i=1}^n (1 + r K_i)^2 + \tau_0 \\ \mu_u^* = \left(\tau_k \sum_{i=1}^n S_i (1 + r K_i) + \tau_0 u_0 \right) / \tau_u^*.$$

4.2. Sampling Algorithm

[33] We sample the joint posterior distribution shown in equation (7) using the Gibbs sampler [Geman and Geman, 1984]. Let $N = \{1, 2, 3, \dots, n\}$ represent the index set of all pixels. The main steps of the sampling approach are given as follows:

[34] 1. Assign initial values to $\{S_j\}$, $\{K_j\}$, u , τ_s , and τ_k and refer to them as $\{S_i^{(0)}\}$, $\{K_i^{(0)}\}$, $u^{(0)}$, $\tau_s^{(0)}$, and $\tau_k^{(0)}$, respectively. Let $p = 1$.

[35] 2. Draw a sample from the normal distribution $[S_i|\cdot]$ in equation (9) and refer to it as $S_i^{(p)}$ for $i \in N$.

[36] 3. Draw a sample from the gamma distributions $[\tau_s|\cdot]$ and $[\tau_k|\cdot]$, and normal distribution $[u|\cdot]$ in equation (18) and refer to them as $\tau_s^{(p)}$, $\tau_k^{(p)}$, and $u^{(p)}$, respectively.

[37] 4. Draw a sample from the Bernoulli distribution $[K_i|\cdot]$ given $S_i^{(p)}$, $u^{(p)}$, $\{K_j^{(p)}\}$, $j = 1, 2, \dots, i-1\}$, and $\{K_j^{(p-1)}\}$, $j = i+1, \dots, n\}$ and refer to it as $K_i^{(p)}$ for $i \in N$.

[38] 5. Let $p = p + 1$. If $p > m$, where m is the maximum number of iterations allowed, stop; otherwise, go to step 2.

4.3. Monitoring Convergence of the Sampling

[39] Samples obtained from the algorithm described in section 4.2 are typically not the samples of their individual posterior distributions. However, theoretically, after a sufficiently long run (for example t iterations), referred to as burn in, $\{S_i^{(k)}, K_i^{(k)}, u^{(k)}, \tau_s^{(k)}, \tau_k^{(k)} : k = t+1, \dots, m, i \in N\}$ obtained from the algorithm are approximately samples from their corresponding true posterior distributions [Gelfand and Smith, 1990]. In addition, as indicated by the ergodicity theorem [Gilks et al., 1996], the mean of any measurable function of those variables obtained using the generated samples after discarding the burn-in samples asymptotically converges to its true expectation as $k \rightarrow +\infty$.

[40] We use the Gelman and Rubin [1992] method to monitor the convergence of the sampling process in this study. We first run several Markov chains [Gilks et al., 1996] with very different initial values, and then calculate a criterion (referred to as the scale reduction score) on the basis of the multiple Markov chains [Brooks and Gelman, 1998]. If the scale reduction score is less than 1.2, the Markov chain is considered convergent; otherwise, more runs are needed.

5. Application to Field Data

[41] We apply our developed joint inversion approach in this section along several cross sections shown in Figure 2. We jointly estimate seismic slowness, the probability of being in the high-conductivity zone, and the unknown parameters associated with petrophysical models by combining crosshole seismic travel time and borehole flowmeter test data.

[42] Figure 9 shows the prior and posterior distributions of the mean seismic slowness (u) in the high-conductivity zone (Figure 9a), of the reverse variance of the seismic slowness (τ_k) in the two conductivity zones (Figure 9b), and of the reverse variance of seismic travel times (Figure 9c), along the geological strike cross section 26-24. We found that the posterior distributions of those parameters are primarily determined by data. Figure 10 shows the inverted mean seismic velocity along the same cross section. There is a low seismic velocity zone in the middle of the cross section, which likely corresponds to the high hydraulic conductivity zone as explained later.

[43] In the following, we show the probability of being in the high-conductivity zone for other cross sections, and discuss the results. To assess the validity of the obtained zonation estimates, we qualitatively compare the images with bromide breakthrough data obtained by conducting a tracer test along the same transect direction.

5.1. Hydrogeological Zonation

[44] Figure 11 shows the probability image of being in the high-conductivity zone along cross section 26-24. This image suggests that there is a highly conductive fractured zone between wells 26 and 24, which we interpret to be the fracture zone. Figures 12, 13, 14, and 15 illustrate the estimated probability of being in the high-conductivity zone along the four geological dip cross sections 107-24, 107-104, 107-103, and 107-109, within the approximate depth intervals between 10 m and 14 m. At the well locations, the indicator values of flowmeter test data are shown, whereas at

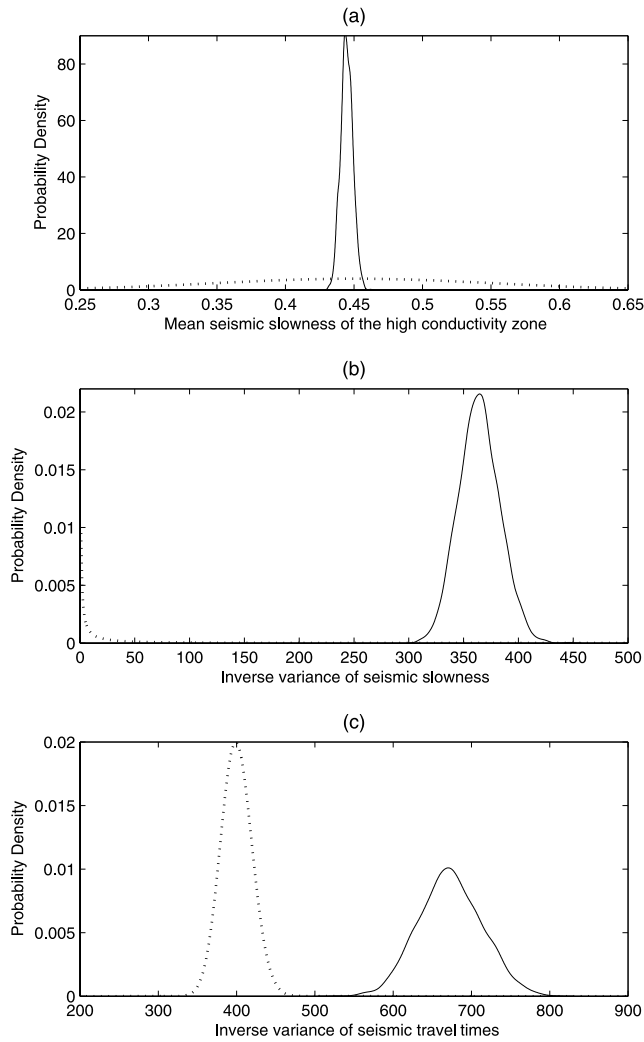


Figure 9. (a) Prior and posterior distributions of the mean seismic slowness in the high-conductivity zone, (b) the reverse variance of seismic slowness in the two conductivity zones, and (c) the reverse variance of seismic travel times along the geological strike cross section 26-24. The dotted lines show the prior probability density functions, and the solid lines show the posterior probability density functions.

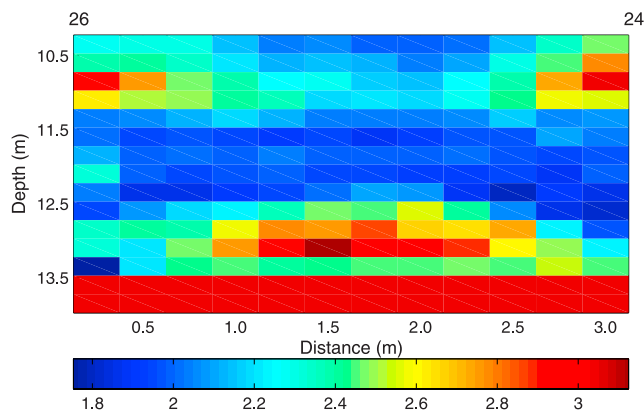


Figure 10. Inverted mean seismic velocity along the geological strike cross section 26-24.

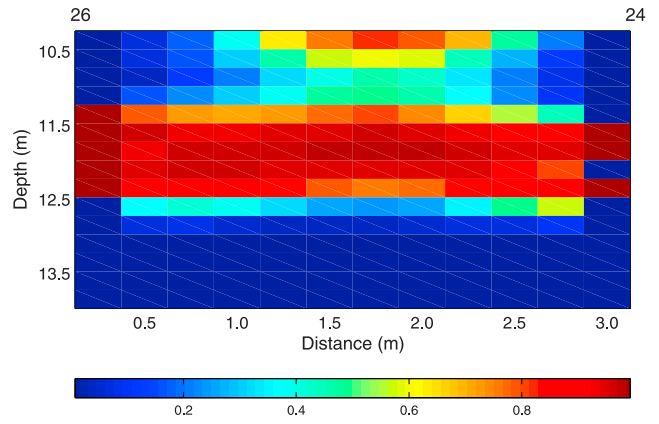


Figure 11. Probability of being in the high-conductivity zone along the geological strike cross section 26-24.

locations away from boreholes, the estimated probabilities of being in the high-conductivity zone are shown. In subsequent cross sections, where borehole deviation data [Geophex, Ltd., 2003] indicate that the boreholes are not vertical, we plot the borehole indicator values along the deviated locations. Recall that the high-conductivity zone refers to areas where the conductivity value greater than 1.0×10^{-4} cm/s. If no crosshole seismic travel time data were available, we would likely just connect the conductive intervals between different wells to obtain estimates of the hydraulic conductivity zonation between the wells. With the incorporation of crosshole seismic travel time data, we obtain a more detailed “image” of conductivity at locations between the wells. For example, the conductivity distributions along cross sections 107-24 (Figure 12) and 107-103 (Figure 14) suggest that a hydraulic connection of the defined high-conductivity zone does not exist between well pairs 107-24 and 107-103, although wells 107, 24, and 103 indicate the presence of continuous high-conductivity zones between depths of 11 m and 12 m. Figures 13 and 15 show the probability images of being in the high-conductivity zone along cross sections 107-104 and 107-109, respectively. We can see that although a conductive layer exists

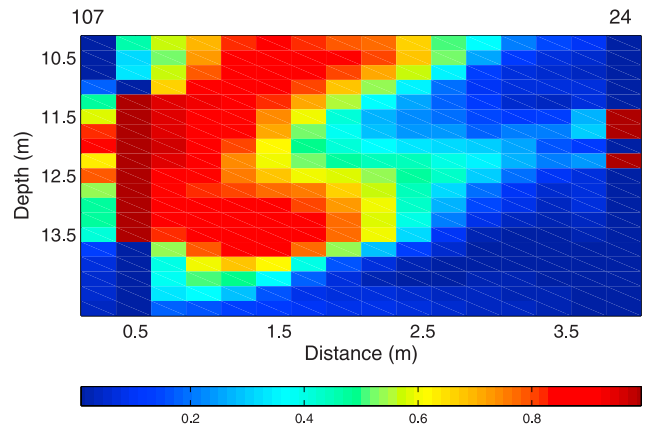


Figure 12. Probability of being in the high-conductivity zone along a geological dip cross section 107-24. The indicator values from flowmeter test data are shown along the borehole locations (well 107 is deviated at depth 10.875 m), whereas estimated probabilities from the joint inversion procedure are shown at all other locations.

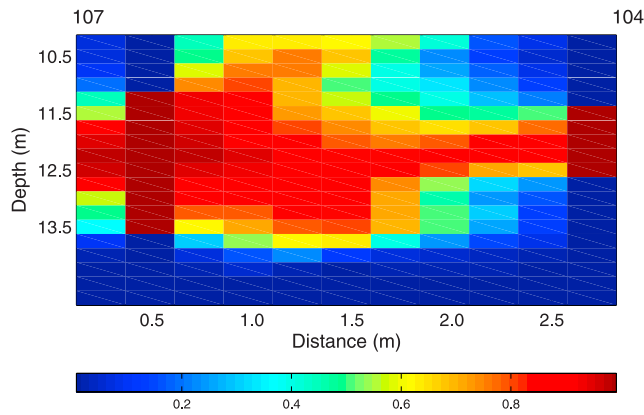


Figure 13. Probability of being in the high-conductivity zone along a geological dip cross section 107-104. The indicator values from flowmeter test data are shown along the borehole locations (well 107 is deviated at depth 8.375 m), whereas estimated probabilities from the joint inversion procedure are shown at all other locations.

between the well pairs along these traverses, the thickness of the zone appears to vary along the lateral direction.

[45] The five probability images delineate the high-conductivity zones at the study site. These images show that the high-conductivity zone, which we interpret to be the fractured zone, is located between depths of 11 m and 12.5 m and is spatially variable. The conductive layer is almost parallel along the direction from well 24 to well 26 (Figure 11). However, as shown by Figures 12–15, the layer dips from Northwest to Southeast and is spatially variable in thickness and in continuity. The hydraulic connection between well 107 and the line from well 24 to well 26 is not uniform as shown in Figures 12–15. Importantly for the biostimulation experiment, the high-conductivity zone is discontinuous between wells 107 and 24 and between wells 107 and 103. In addition, the conductive layer is thicker

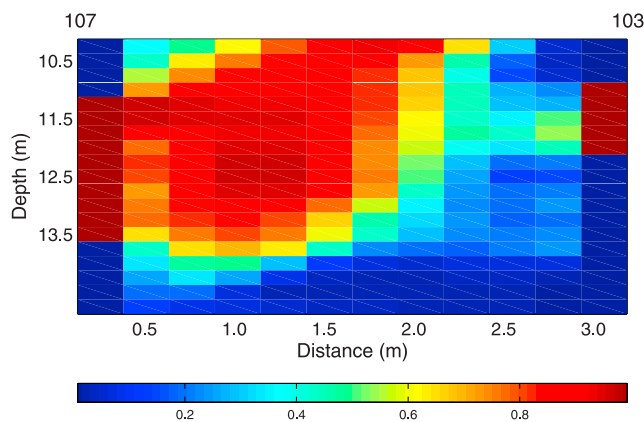


Figure 14. Probability of being in the high-conductivity zone along a geological dip cross section 107-103. The indicator values from flowmeter test data are shown along the borehole locations, whereas estimated probabilities from the joint inversion procedure are shown at all other locations.

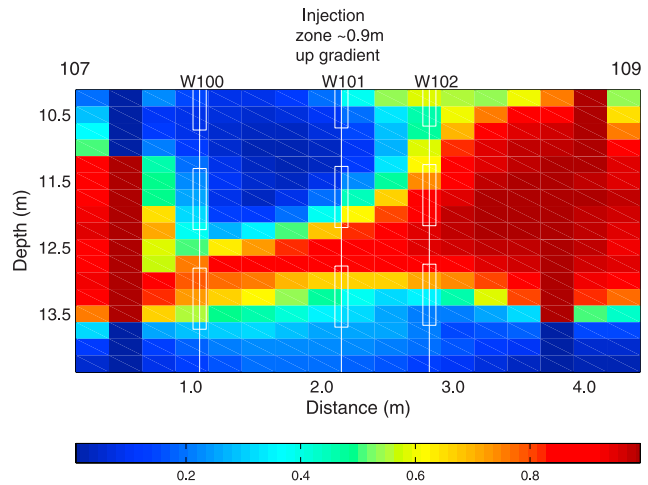


Figure 15. Probability of being in the high-conductivity zone along a geological dip cross section 107-109. The indicator values from flowmeter test data are shown along the borehole locations, whereas estimated probabilities from the joint inversion procedure are shown at all other locations. Well 107 is deviated at depth 8.375 m, and well 109 is deviated at depths 6.875 and 11.375 m. The three lines with boxes represent the projected locations of observation wells 100, 101, and 102 on cross section 107-109. The boxes represent the multiple sampler intervals used during the field bromide tracer and uranium biostimulation experiments. The center depths of the intervals from the top to the bottom are about 10.2, 11.7, and 13.2 m, respectively.

toward wells 108 and 109 than toward well 107 as shown in Figure 15.

5.2. Comparison With Field Tracer Experiments

[46] To qualitatively assess the joint inversion procedure, we compare the probability images with the results of a field tracer experiment carried out at the site, as well as with observations associated with the biostimulation experiment [Wu *et al.*, 2006a]. To develop a forced gradient, groundwater was injected into well 24 (2.36 liter/min) and well 104 (4.0 liter/min), and pumped out from well 103 (1.4 liter/min) and well 26 (3.0 liter/min). A bromide tracer was injected into well 104 within the conductive zone, and the breakthrough concentrations were measured over time using multilevel samplers at wells 100, 101, and 102. As shown in Figure 2, well 101 is located directly down gradient (0.9 m) (or downdip along strike) from the tracer injection well 104, and wells 100 and 102 are located along the strike downdip and updip of the injection flow path, respectively. There are seven ports in each of the multilevel sampling wells, but only the deepest three registered a significant bromide concentration response. From the top to the bottom, the depths of the center locations of the three deepest sampling intervals are 10.2 m, 11.7 m, and 13.2 m, respectively. Figure 15 shows the approximate locations of the multilevel sampling wells, superimposed on the top of the estimated probability values along the cross section 107-109.

[47] Figure 16 shows the relative bromide concentrations collected from those samplers at wells 100, 101, and 102 over time. Although the observation wells are not directly on cross section 107-109, we can project them to the plane

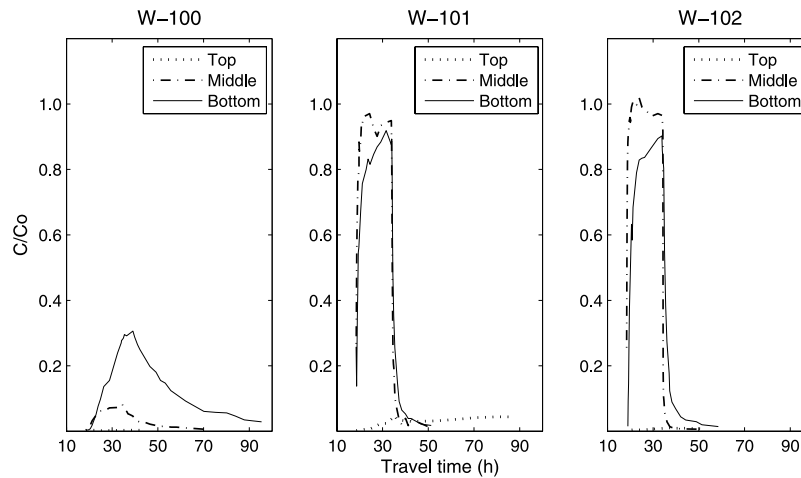


Figure 16. Recorded bromide concentrations versus travel times at observation wells 100, 101, and 102 [Wu *et al.*, 2006a]. The dotted, dashed, and solid lines represent data obtained from the top, middle, and bottom sampler intervals, respectively.

(Figure 2), as is illustrated by the boxes in Figure 15. By comparing Figures 15 and 16, we find that the estimated hydrogeological zonation structure, described in section 5.1 and provided by the joint inversion approach, is useful for understanding the tracer experiment results. Without the tomographic information, we would expect that under forced gradient conditions, the injected tracer would move along the injection centerline, possibly migrate slightly down to geological dip or the Southeast direction, and be relatively evenly distributed about the centerline of the flow field. Instead, Figure 16 shows that little tracer arrived at the downdip sampling well 100, and what did arrive there did so later in time than at the other samplers. In all the sampling wells, only minor tracer was detected in the top samplers. The middle samplers on wells 101 and 102 received most of the tracer, and the tracer arrived at those ports about the same time as each other and earlier than all other arrivals. This asymmetry is in part due to the misalignment of the wells [Fienen *et al.*, 2005] and in part due to the discontinuity of the high-conductivity zone in the region of well 100 as illustrated by the results of the inversion method. The bromide breakthrough at the middle ports in wells 101 and 102 was almost immediately followed by the breakthrough in the lower samplers of those wells. Similar results were also observed during the uranium (VI) tracer experiments [Wu *et al.*, 2006a, 2006b]. The nutrients injected at well 104 as part of the biostimulation experiment have never been observed in well 100, which suggests that this zone is hydraulically isolated from the injection well as was suggested by the tomographic information. These results highlight the importance of heterogeneity on transport and remediation efficacy.

[48] As shown in Figure 15, since the centers of all the top samplers are outside the conductive layer, the observed bromide concentrations within the top samplers are low in each observation well. Again, as shown in Figure 15, the middle samplers of wells 101 and 102 are within the conductive layer, and thus we observe large concentrations along those wells. For the bottom samplers, we also

observed high concentrations in those samplers that are near the conductive layers. Since the thickness of the high-conductivity layer in Figure 15 is greater near well 102, we might expect more breakthrough near that well than well 101. However, well 101 is directly down gradient (0.9 m) from the injection well 104. Consequently, the shorter travel path to well 101 and the larger high-conductivity zone associated with well 102 likely result in the tracer arriving at the two wells at approximately the same time.

[49] Although the qualitative comparison of the estimated zonation with the tracer and biostimulation observations is reasonable, there are some minor discrepancies. Several reasons may explain the disparities. For example, the locations of wells 100, 101, and 102 shown on cross section 107-109 are projected onto the cross section, which may account for small difference between the expected and observed results. Additionally, the probability images are sensitive to the given cutoff value; higher cutoff values would have resulted in a smaller estimated high-conductivity zone, whereas lower values would have resulted in a larger zone. Nonetheless, the obtained estimates agree well with the transport observations and suggest the importance of heterogeneity on tracer transport and remediation results.

6. Summary

[50] We have developed a joint inversion approach in this study to combine crosshole seismic travel time and borehole flowmeter test data, and have applied the developed method to a real data set to estimate the zonation of high hydraulic conductivity that we interpret to be the fracture zone. While conventional hydrogeophysical two-step estimation approaches are not viable at this site because of the poor cross correlation between the inverted seismic velocity and hydraulic conductivity (Figure 4), our joint inversion approach provided reasonable estimates of hydrogeological zonation structure on the basis of a qualitative comparison of the obtained estimates with the results of field tracer and uranium biostimulation experiments. For applications of the methodology to other sites, several assumptions can be

relaxed, depending on data quality and specific field situations. Estimates of continuous values or other types of categorical values of hydraulic conductivity can be obtained by using a more complicated petrophysical model. In those cases, a procedure, similar to the one shown in this study, can be used to develop a sampling-based Bayesian model for solving the complex characterization problem.

[51] The joint inversion approach is expected to be more effective for combining different types of data sets than conventional sequential estimation approaches because the approach permits information sharing between hydrogeological and geophysical data, which may lead to the reduction of uncertainty in both geophysical data inversion and hydrogeological parameter estimation. For example, in this study, the estimates of seismic slowness at pixels near boreholes benefit from proximal borehole flowmeter test measurements. The developed approach is also flexible; it allows us to use petrophysical models with unknown parameters, so that we can consider the effects of uncertainty in petrophysical models and in geophysical inversion together on the estimates of hydrogeological parameters. For example, the estimated probability images of being in the high-conductivity zone reflect the effects of uncertainty in both the petrophysical model and the travel time data inversion. In addition, since we use a sampling-based Bayesian model, complex numerical simulation models can also be incorporated into the joint inversion approach. Our study suggests that the developed joint hydrogeophysical inversion approach is effective for integrating various types of data sets within complex subsurface environment, and that seismic travel time data have the potential to provide valuable information about fracture zonation.

[52] **Acknowledgments.** Funding for this study was provided by the Natural and Accelerated Bioremediation Research (NABIR) Program of the Environmental Remediation Science Division, the U.S. DOE Office of Science, to Susan Hubbard. The authors wish to thank Tonia Mehlhorn from the Oak Ridge National Laboratory for providing the tracer test data and Peter Kitanidis and Craig Criddle from Stanford University for allowing us to participate in the project.

References

- Bernardo, J. M., and A. F. Smith (1994), *Bayesian Theory*, John Wiley, Hoboken, N. J.
- Binley, A., P. Winship, R. Middleton, M. Pokar, and J. West (2001), High-resolution characterization of vadose zone dynamics using cross-borehole radar, *Water Resour. Res.*, *37*(2), 2639–2652.
- Bosch, M., A. Guillen, and P. Ledru (2001), Lithologic tomography: An application to geophysical data from the Cadomian belt of northern Brittany, France, *Tectonophysics*, *31*, 197–227.
- Brooks, S. P., and A. Gelman (1998), General methods for monitoring convergence of iterative simulation, *J. Comput. Graphical Stat.*, *7*(4), 434–455.
- Buland, A., and H. Omre (2003), Joint aVO inversion, wavelet estimation and noise-level estimation using a spatially coupled hierarchical Bayesian model, *Geophys. Prospect.*, *51*, 531–550.
- Cassiani, G., G. Bohm, A. Vesnaver, and R. Nicolich (1998), A geostatistical framework for incorporating seismic tomography auxiliary data into hydraulic conductivity estimation, *J. Hydrol.*, *206*, 58–74.
- Chen, J., and Y. Rubin (2003), An effective Bayesian model for lithofacies estimation using geophysical data, *Water Resour. Res.*, *39*(5), 1118, doi:10.1029/2002WR001666.
- Chen, J., S. Hubbard, and Y. Rubin (2001), Estimating the hydraulic conductivity at the South Oyster site from geophysical tomographic data using Bayesian techniques based on the normal linear regression model, *Water Resour. Res.*, *37*(6), 1603–1613.
- Chen, J., S. Hubbard, Y. Rubin, C. Murray, E. Roden, and E. Majer (2004), Geochemical characterization using geophysical data and Markov chain Monte Carlo methods: A case study at the South Oyster bacterial transport site in Virginia, *Water Resour. Res.*, *40*, W12412, doi:10.1029/2003WR002883.
- Criddle, C., et al. (2003), Biostimulation of uranium reduction in situ and coupled ex situ ground water treatment at the NABIR Field Research Center, paper presented at DOE-NABIR PI Workshop, Dep. of Energy, Warrenton, Va., 17–19 March.
- Day-Lewis, F. D., and J. W. Lane Jr. (2004), Assessing the resolution-dependent utility of tomograms for geostatistics, *Geophys. Res. Lett.*, *31*, L07503, doi:10.1029/2004GL019617.
- Doll, W. E., D. B. Watson, and P. M. Jardine (2002), Geophysical profiling in support of a nitrate and uranium groundwater remediation study, paper presented at 2002 Symposium on the Application of Geophysics to Engineering and Environmental Problems, Environ. and Eng. Geophys. Soc., Las Vegas, Nev., 10–14 Feb.
- Ellefson, K. J., P. A. Hsieh, and A. M. Shapiro (2002), Crosswell seismic investigations of hydraulically conductive, fractured bedrock near Mirror Lake, New Hampshire, *J. Appl. Geophys.*, *50*, 299–317.
- Fienen, M. N., P. K. Kitanidis, D. Watson, and P. Jardine (2004), An application of Bayesian inverse methods to vertical deconvolution of hydraulic conductivity in a heterogeneous aquifer at Oak Ridge National Laboratory, *Math. Geol.*, *36*(1), 101–126.
- Fienen, M. N., J. Luo, and P. K. Kitanidis (2005), Semi-analytical, homogeneous, anisotropic capture zone delineation, *J. Hydrol.*, *312*, 39–50.
- Gelfand, A. E., and A. F. M. Smith (1990), Sampling-based approaches to calculating marginal densities, *J. Am. Stat. Assoc.*, *85*(410), 398–409.
- Gelman, A., and D. B. Rubin (1992), Inference from iterative simulation using multiple sequences, *Stat. Sci.*, *7*(4), 457–472.
- Geman, S., and D. Geman (1984), Stochastic relaxation, Gibbs distributions, and the Bayesian restoration of images, *IEEE Trans. Pattern Anal. Mach. Intel.*, *6*, 721–741.
- Geophex, Ltd. (2003), Borehole Geophysical Services, Area 3, DOE Y-12 Facility, technical report, Oak Ridge, Tenn.
- Gilks, W. R., S. Richardson, and D. J. Spiegelhalter (1996), *Markov Chain Monte Carlo in Practice*, CRC Press, Boca Raton, Fla.
- Hubbard, S., Y. Rubin, and E. Majer (1997), Ground penetrating radar assisted saturation and permeability estimation in bimodal systems, *Water Resour. Res.*, *33*(5), 971–990.
- Hyndman, D. W., J. M. Harris, and S. M. Gorelick (1994), Coupled seismic and tracer test inversion for aquifer property characterization, *Water Resour. Res.*, *30*(7), 1965–1977.
- Illman, W. A. (2005), Type curve analyses of pneumatic single-hole tests in unsaturated fractured tuff: Direct evidence for a porosity scale effect, *Water Resour. Res.*, *41*, W04018, doi:10.1029/2004WR003703.
- Illman, W. A., and S. P. Neuman (2000), Type-curve interpretation of multi-rate single-hole pneumatic injection tests in unsaturated fractured rock, *Ground Water*, *38*(6), 899–911.
- Kowalsky, M. B., S. Finsterle, and Y. Rubin (2004), Estimating flow parameter distributions using ground-penetrating radar and hydrological measurements during transient flow in the vadose zone, *Adv. Water Resour.*, *27*, 583–599.
- Linde, N., J. Chen, M. Kowalsky, and S. Hubbard (2006), Hydrogeophysical parameter estimation approaches for field scale characterization, in *Applied Hydrogeophysics*, Springer, New York, in press.
- Majer, E. L., L. R. Myer, J. E. Peterson, K. Karasaki, J. C. S. Long, S. J. Martel, P. Blumling, and S. Vomvoris (1990), Joint seismic, hydrogeological, and geomechanical investigations of a fracture zone in the Grimsel Rock Laboratory, Switzerland, technical report, Lawrence Berkeley Natl. Lab., Berkeley, Calif.
- Majer, E. L., J. E. Peterson, T. Daley, B. Kaelin, L. Myer, J. Queen, P. D'Onfro, and W. Rizer (1997), Fracture detection using crosswell and single well surveys, *Geophysics*, *62*, 495–504.
- Malinverno, A. (2002), Parsimonious Bayesian Markov chain Monte Carlo inversion in a nonlinear geophysical problem, *Geophys. J. Int.*, *151*, 675–688.
- Molz, F., G. Boman, S. Young, and W. Waldrop (1994), Borehole flowmeters: Field application and data analysis, *J. Hydrol.*, *163*, 347–371.
- Peterson, J. E. (2001), Pre-inversion processing and analysis of tomographic radar data, *J. Environ. Eng. Geophys.*, *6*(1), 1–18.
- Peterson, J. E., B. N. Paulsson, and T. V. McEvelly (1985), Applications of algebraic reconstruction techniques to crosshole seismic data, *Geophysics*, *50*, 1566–1580.

- Pyrak-Nolte, L. J., L. R. Myer, and N. G. W. Cook (1990), Transmission of seismic waves across single natural fractures, *J. Geophys. Res.*, 95(B6), 8617–8638.
- Vasco, D. W., J. E. Peterson, and E. L. Major (1996), A simultaneous inversion of seismic traveltimes and amplitudes for velocity and attenuation, *Geophysics*, 61, 1738–1757.
- Watson, D., W. Doll, J. Gamey, J. Sheehan, and P. Jardine (2005), Plume and lithologic profiling with surface resistivity and seismic tomography, *Ground Water*, 43(2), 169–177.
- Wu, W.-M., et al. (2006a), Field-scale of bioremediation of uranium in a highly contaminated aquifer I: Conditioning of a treatment zone, *Environ. Sci. Technol.*, in press.
- Wu, W.-M., et al. (2006b), Field-scale of bioremediation of uranium in a highly contaminated aquifer II: Geochemical control of U (VI) bioavailability and evidence of U (VI) reduction, *Environ. Sci. Technol.*, in press.
-
- J. Chen, S. Hubbard, J. Peterson, and K. Williams, Lawrence Berkeley National Laboratory, Berkeley, CA 94720, USA. (jchen@lbl.gov)
- M. Fienen, Department of Civil and Environmental Engineering, Stanford University, Stanford, CA 94305-4020, USA.
- P. Jardine and D. Watson, Environmental Sciences Division, Oak Ridge National Laboratory, Oak Ridge, TN 37831-6038, USA.